ITC 1/52
Information Technology and Control
Vol. 52 / No. 1 / 2023
pp. 37-52
DOI 10.5755/j01.itc.52.1.31520

A Neutrosophic Set Approach on Chest X-rays for Automatic Lung Infection Detection

Received 2022/05/30 | Accepted after revision 2022/07/22

https://doi.org/10.5755/j01.itc.52.1.31520

HOW TO CITE: Sofia Jennifer, J., Sree Sharmila, T. (2023). A Neutrosophic Set Approach on Chest X-rays for Automatic Lung Infection Detection. *Information Technology and Control*, 52(1), 37-52. https://doi.org/10.5755/j01.itc.52.1.31520

A Neutrosophic Set Approach on Chest X-rays for Automatic Lung Infection Detection

Sofia Jennifer J., Sree Sharmila T.

Department of Information Technology; Sri Sivasubramaniya Nadar College of Engineering, Kalavakkam, Chennai, India

Corresponding author: sofiajenniferj@ssn.edu.in

COVID cases and its variants is noted enormously in the past three years. In many medical cases, lung infections such as viral pneumonia, bacterial pneumonia have been initially interpreted as COVID-19. Hence, the proposed work is concentrating on differentiating these lung infection types. This work focuses on using neutrosophic approach of classifying into True (T), False (F) and Indeterminacy (I) set membership to reduce the fuzziness and retain more significant information for feature extraction of the opacity to differentiate the types of lung infections. Initially, the images are preprocessed by alpha-mean and beta- enhancement operation to reduce the indeterminacy and enhancing the image components as the range of lung opacity levels to determine the types. Then, these neutrosophic set enhanced images are fed to various deep learning models like ResNet-50, VGG-16 and XGBoost for classification. Experiments are conducted on ActualMed COVID-19 Chest X-ray and COVID-19 radiography dataset and a comparative analysis on several domain set of images such as the original image, neutrosophic domain (T, I, F) and enhanced neutrosophic domain (alpha, beta) are trained and tested through transfer learning by tuning the various validation parameters. On experimental analysis, an enhanced neutrosophic image achieves a better accuracy of 97.33% among the other domain sets.

KEYWORDS: Deep Learning, Enhancement Technique, Lung Infections, Neutrosophic Sets, X-Ray Images.

1. Introduction

The COVID-19 pandemic continues to have a devastating effect on the health and wellbeing of the global population. COVID cases and its mutant forms is still a threat in today's scenario. Chest X-ray is considered to the first imaging technique and the easily available tool for diagnosis [22]. Many underdeveloped countries where CT-scan facility is not available, X-rays are still used to predict the stage of COVID infections [25].

In medical science, the X-ray images consist of fuzzy and imprecision information that makes segmentation and classification a difficult task [26]. Thus, the generalizations of fuzzy sets are generally used to reduce the fuzziness and uncertainty in images and many studies have concluded that the fuzzy theory on image enhancement retains more significant information than traditional methods [18]. These fuzzy methods fail to consider the spatial pixel data due to noise and artifacts which play a vital role in many real-time applications. To resolve this issue, neutrosophic set is the better way to quantify the images with the usage of indeterminacy.

By standard definition, Neutrosophic set (NS) is a subset of neutrosophy theory and it studies the origin, nature, and scope of neutralities, as well as their interaction with different ideational spectra [5]. The NS further enhances the independent uncertainty measures by generalizing into truth, indeterminacy, and falsity membership. The proposed idea focuses on using neutrosophic approach to reduce the fuzziness and retain more significant information for feature extraction of the opacity to differentiate the types of lung infections such as normal, viral, and bacterial pneumonia and COVID-19 infection.

Many existing research on lung infection detection are done using either traditional image segmentation or deep learning approaches. In deep learning approach, the images are pre-processed and directly fed to the CNN model. During the preprocessing step, there is a loss of essential information. As the classification is based on the differences in the density of the lung opacity (hazy gray areas around the lungs), every pixel holds significant information and hence neutrosophic set is used in the proposed model. To further increase the accuracy alpha mean and beta enhancement is done.

1.1. Motivation, Objectives, Contributions, and Organization

In many medical cases, lung infections such as viral pneumonia, bacterial pneumonia have been initially interpreted as COVID-19. Hence, the motivation of the proposed model is to differentiate the lung infection types.

The main objective of this approach is to retain the pixel essential information about the density of the lung opacity by using neutrosophic set and then train and test them in a deep learning environment.

The proposed method focuses on the following three steps: (i) The input Chest X-ray images are converted to neutrosophic domain with True (T), False (F) and Indeterminacy (I) set images, (ii) Two operations such as α-mean and β-enhancement operations are used to reduce the set indeterminacy to further enhance the image edges to improve accuracy, and (iii) The enhanced images are fed into the transfer learning architectures such as ResNet-50, VGG-16 and XG-Boost to train and test for the type of lung infections.

The rest of the of the paper is organized as follows: A study on the existing methods is mentioned in Section 2. The proposed methodology is explained in Section 3. Section 4 of this paper explains the results of the experiment carried out using proposed method. Conclusion of this work is discussed in Section 5.

2. Related Works

Studies diagnosed with COVID-19 using chest X-rays have mostly binary classifications. Some studies use raw data while others have feature extraction process in deep learning. With transfer learning, the detection of various abnormalities in small medical image datasets holds remarkable results.

Based on chest X-ray images, Zhang [28] aimed to develop a deep learning-based model that can detect COVID-19 with high sensitivity, providing fast and reliable scanning. Ayan [2] proposed a diagnosis system for pneumonia chest x-ray images using existing deep learning models. This diagnosis system uses an X- ray data set [19] that contains 1600 healthy cases

and 4200 un-healthy pneumonia cases. The model used is VGG and X-ception where VGG holds an error rate of 19%. Alqudah [1] worked on two different methods to diagnose COVID-19 using chest X-ray images. Firstly, with market available deep learning models AOCTNet, MobileNet and ShuffleNet CNNs. Secondly, by removing the features of the input images and then classify using softmax classifier, k-nearest neighbor (kNN), support vector machine (SVM) and random forest (RF) algorithms [1]. Korkmaz used the SqueezeNet model with Bayesian optimization [25]. Barstugan [3] used five different feature extraction method such as Grey Level Cooccurrence Matrix (GLCM), Local Directional Patterns (LDP), Grey Level Run Length Matrix (GLRLM), Grey Level Size Zone Matrix (GLSZM), and Discrete Wavelet Transform (DWT) and then classified using SVM.

In a deep learning approach, to minimize the training process and implementation of neural networks, collaborative training called federated learning (FL) was proposed [30]. This federated learning approach uses many workers for training on small, private databases and to create one aggregated model. Another major problem in deep learning is handling of misclassifications. Dawid [8] proposes the idea of rewards and penalties and this approach improves the accuracy, reducing the chance of obtaining erroneous information.

All the existing methods use raw data but since X-ray images holds many fuzzy and imprecision information, a lot of preprocessing is done to achieve better classification accuracy. In [19], the use of three methods like neural network, heuristic and fuzzy logic for damage detection to rectify the fuzziness and hold essential information. The fuzzy consensus with federated learning approach has been recent addiction that has been used for decision-making in medical systems [21].

In this paper, neutrosophic set is used to retain persistent information with the usage of indeterminacy. The author [22] has introduced the idea of using the significance of neutrosophic sets on various deep transfer learning models like Alexnet, Googlenet, and Restnet18 for COVID-19 detection. The approach failed to enhance the images as each pixel value is essential to handle data uncertainties.

3. Neutrosophic Set Approach for Lung Infection Detection

The proposed Neutrosophic set approach on deep learning architecture for lung infection detection is described in block diagram as shown in Figure 1: (i) Image dataset acquisition (ii) Preprocessing the image (iii) Training the model and (iv) Testing the unseen images.

Figure 1

Proposed Neutrosophic set approach for lung infection detection

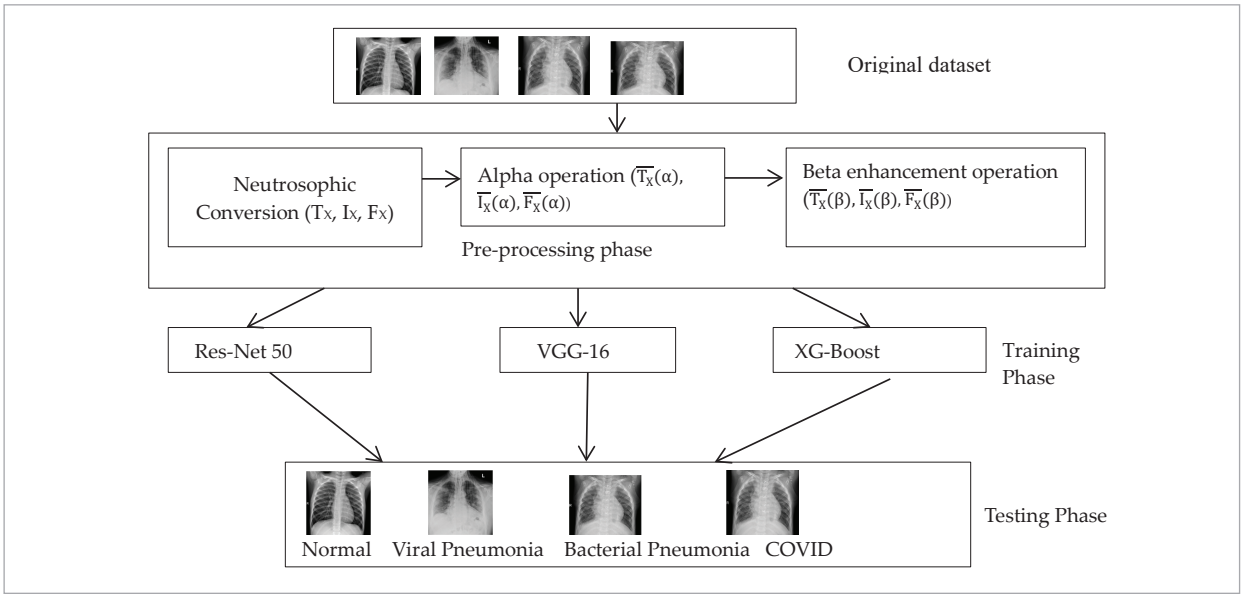

Figure 2
Sample Chest X-ray Images (a) Normal (b) COVID-19 (c) Viral Pneumonia (d) Bacterial Pneumonia

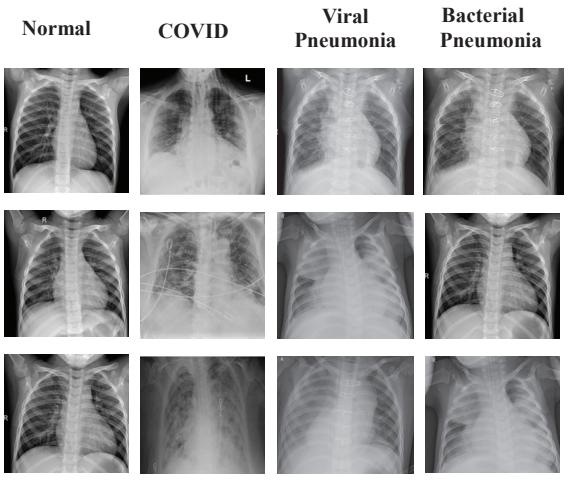

3.1. Neutrosophic Domain

3.1.1 Neutrosophic Set

Neutrosophy is the study of origin, nature, and scope of neutralities. This branch is an extension of fuzzy logic or set and is generalized as neutrosophic set similarity [17]. The definition, concepts and properties of neutrosophic set (NS) are mentioned in many research papers [27, 5].

Definition 3.1.1. Neutrosophic set (NS): Consider Z to be a universe of discourse and a neutrosophic set S is a part of Z. An element z in set A is denoted in mathematical terms as z (t, i, f) and represented in NS logic using Equation 1:

$$S = \left\{ \left[z, \left(T_S(z), I_S(z), F_S(z) \right) \right] z \in Z \right\}, \quad (1)$$

where $T_S(z)$, $I_S(z)$ and $F_S(z)$ are the neutrosophic components and are real standard or non-standard sets of $]0^-, 1^+[$ and is defined using Equations (2)-(3).

$$n_{\sup} = t_{\sup} + i_{\sup} + f_{\sup}, \quad (2)$$

where
$\sup\_T = t_{\sup}, \sup\_I = i_{\sup}, \sup\_T = f_{\sup}$

$$n_{\inf} = t_{\inf} + i_{\inf} + f_{\inf}, \quad (3)$$

where $\inf T = t_{inf}$, $inf\,\mathrm{I} = \mathrm{i}_{\inf}$, $\inf\_\mathrm{F} = \mathrm{F}_{\inf}$,

so, $0^- \leq T_S(z) + I_S(z) + F_S(z) \leq 3^+$

In the above equations T, I and F are defined as the degree of the true, indeterminate and false membership function of set A, respectively [19]. An element x(t, i, f) belongs to set A and is represented in the following way: t% true, i% indeterminacy, and f% false. In this t varies in T, i varies in I, and f varies in F domain [20].

3.1.2. Neutrosophic Images

In neutrosophy, for any image-based application, the image from spatial domain is represented as a neutrosophic image as follows:

Definition 3.1.2. Neutrosophic image (NI): Consider Z to be a universe of the discourse and the image window W = w * w i.e., rows and columns in spatial domain. Thus, W is a collection of image intensity pixels, where W ⊆ Z and it holds with bright pixels [13]. As per the Equation (4), the neutrosophic image is generally characterized by three membership sets T, I and F [12]. For the proposed image with dimensions M * N, each pixel $P_T(m, n)$ is represented as $P_{NS}(m, n)$ in the neutrosophic image. $P_{NS}(m, n)$ interpret the memberships to bright, indeterminate and black intensity values through true $T_T(m, n)$, indeterminate $I_T(m, n)$ and false $F_T(m, n)$ as portrayed in Figure 3. It is represented using the following Equations (5)-(7). [12]:

$$P_{NS}(m,n) = \left\{ T_T(m,n), I_T(m,n), F_T(m,n) \right\} \quad (4)$$

$$T_T(m,n) = \frac{\overline{g(m,n)} - \overline{g_{\min}}}{\overline{g_{\max}} - \overline{g_{\min}}} \quad (5)$$

where,

$$\overline{g(m,n)} = \frac{1}{w*w} \sum_{x=m-\frac{w}{2}}^{m+\frac{w}{2}} \sum_{y=n-\frac{w}{2}}^{n+\frac{w}{2}} g(x,y)$$

$$I_T(m,n) = \frac{\delta(m,n) - \delta_{\min}}{\delta_{\max} - \delta_{\min}}, \quad (6)$$

where, $\delta(m,n) = abs(g(m,n) - \overline{g(m,n)})$

$$F_T(m,n) = 1 - T_T(m,n), \quad (7)$$

where, g(m, n) – image's local mean value. δ(m, n) – the absolute difference between pixel intensity g(m, n) and mean value g(m, n).

Figure 3

T_T, I_T, F_T domain images of (a) Normal (b) COVID-19 (c) Viral Pneumonia (d) Bacterial Pneumonia

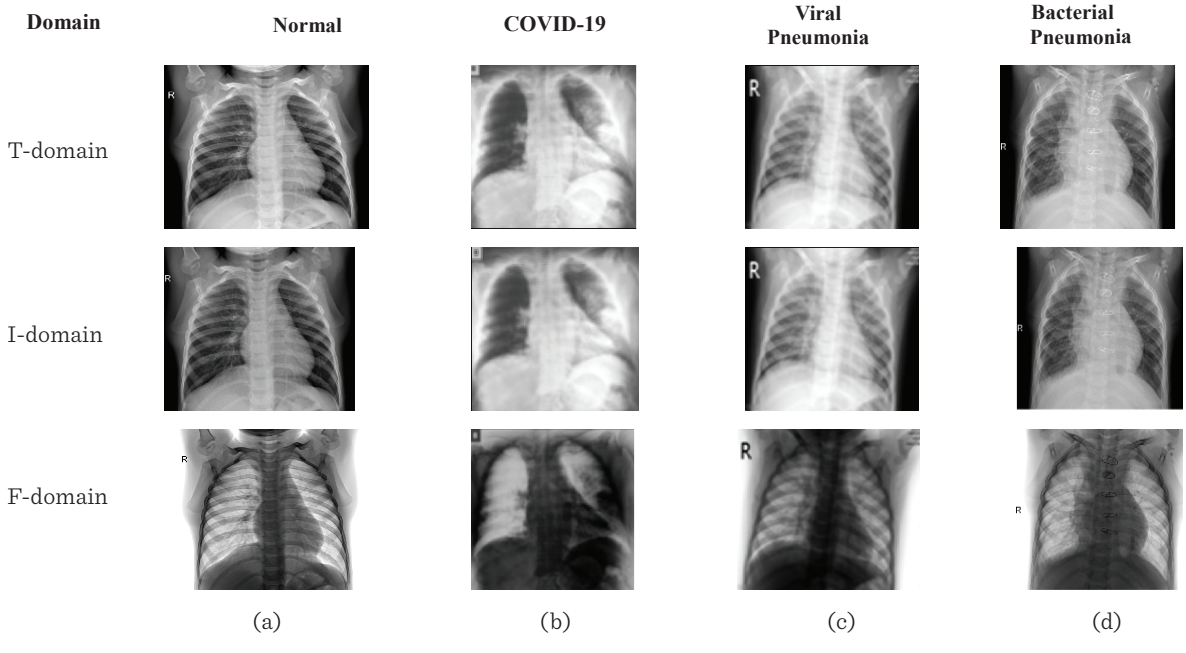

3.1.3. Alpha Mean Operation

Definition 3.1.3. The α -mean operation for P_{NFS}= P (T_T, I_T, F_T) and is defined as Equations (8)-(14) [6, 14].

$$P_{NFS}(\alpha) = \{T_T(\alpha), I_T(\alpha), F_T(\alpha)\} \tag{8}$$

The True mean set

$$\overline{T_T}(\alpha) = \begin{Bmatrix} T_T & if\ I_T < \alpha \\ \overline{T}_T & if\ I_T \geq \alpha \end{Bmatrix}, \tag{9}$$

where,

$$\overline{T_T(m,n)} = \frac{1}{w*w} \sum_{x=m-\frac{w}{2}}^{m+\frac{w}{2}} \sum_{y=n-\frac{w}{2}}^{n+\frac{w}{2}} T_T(x,y) \tag{10}$$

The False mean set

$$\overline{F_T}(\alpha) = \begin{Bmatrix} F_T & if\ I_T < \alpha \\ \overline{F}_T & if\ I_T \geq \alpha \end{Bmatrix}, \tag{11}$$

where,

$$\overline{F_T(m,n)} = \frac{1}{w*w} \sum_{x=m-\frac{w}{2}}^{m+\frac{w}{2}} \sum_{y=n-\frac{w}{2}}^{n+\frac{w}{2}} F_T(x,y) \cdot \tag{12}$$

The α value usually ranges within 0 to 1. For experimentation, various α values have been worked on, where α =0.9 holds promising results for the input images. The indeterminate mean set is defined as follows using Equation (13):

$$\overline{I_T}(\alpha) = \overline{I_T}(m,n) = \frac{\overline{\delta(m,n)} \quad \overline{\delta_{\min}}}{\overline{\delta_{\max}} - \overline{\delta_{\min}}}, \tag{13}$$

where, $\delta(m,n) = abs(\overline{T}_T(m,n) - \overline{\overline{T_T(m,n)}})$

$$\overline{\overline{T_T}}(m,n) = \frac{1}{w*w} \sum_{x=m-\frac{w}{2}}^{m+\frac{w}{2}} \sum_{y=n-\frac{w}{2}}^{n+\frac{w}{2}} \overline{T}_T(x,y). \tag{14}$$

At the end of α -mean operation, among the NS images, the indeterminate image shows a uniform distri-

bution of the pixel intensity values as shown in Figure 4 (a)-(d).

3.1.4. Beta-enhancement Operation

Definition 2.1.4. The β -enhancement operation for $P_{NFS} = P(T_T, I_T, F_T)$ is defined as Equations (15)-(21).

$$P'_{NFS}(\beta) = \{T'_T(\beta), I'_T(\beta), F'_T(\beta)\} \quad (15)$$

The True beta mean set is calculated as follows:

$$T'_T(\quad) = \begin{Bmatrix} T_T & if\ I_T \\ T' & if\ I_T \geq \end{Bmatrix} \quad (16)$$

Where,

$$T'_\beta(m,n) = \begin{cases} 2T_T^{\,2}(m,n) & if\ T_T(m,n) \leq 0.5 \\ 1-2(1-T_T(m,n))^2 & if\ T_T(m,n) > 0.5 \end{cases} \quad (17)$$

The False beta mean set is calculated as follows:

$$F'_T(\beta) = \begin{Bmatrix} F_T & if\ I_T < \beta \\ F'_\beta & if\ I_T \geq \beta \end{Bmatrix}. \quad (18)$$

The β value usually ranges within the interval 0 to 1. For experimentation trials, various β values are computed, where α =0.85 yields good outcomes for input alpha images.The Indeterminate mean set is calculated as follows:

$$F'_\beta(m,n) = \begin{cases} 2F_T^{\,2}(m,n) & if\ F_T(m,n) \leq 0.5 \\ 1-2(1-F_T(m,n))^2 & if\ F_T(m,n) > 0.5 \end{cases} \quad (19)$$

The β value usually ranges within the interval 0 to 1. For experimentation trials, various β values are computed, where α =0.85 yields good outcomes for input alpha images. The Indeterminate mean set is calculated as follows:

$$I'_T(\beta) = I'_T(m,n) = \frac{\delta'(m,n) - \delta'_{\min}}{\delta'_{\max} - \delta'_{\min}}, \quad (20)$$

Figure 4

Alpha mean operation: (a) $T_T(\alpha)$ domain (b) $I_T(\alpha)$ domain (c) $F_T(\alpha)$ domain

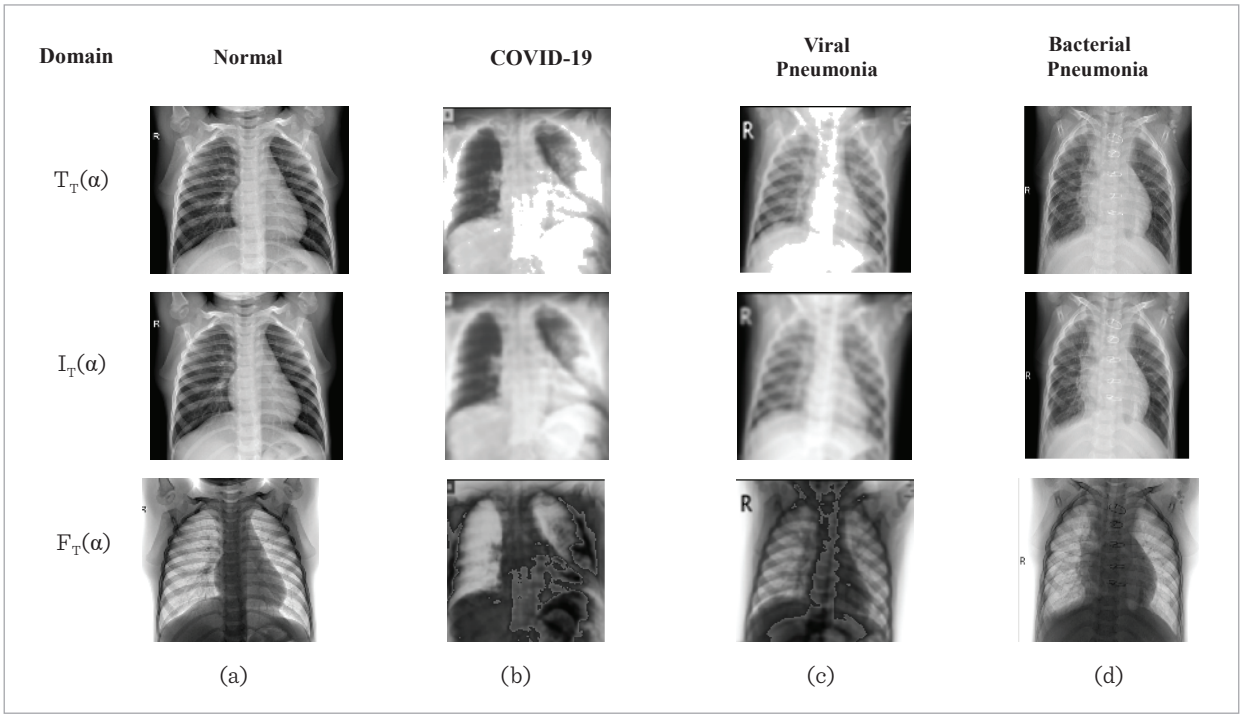

Figure 5
Beta enhancement operation: (a) $T_T^{`}(\beta)$ domain (b) $I_T^{`}(\beta)$ domain (c) $F_T^{`}(\beta)$ domain

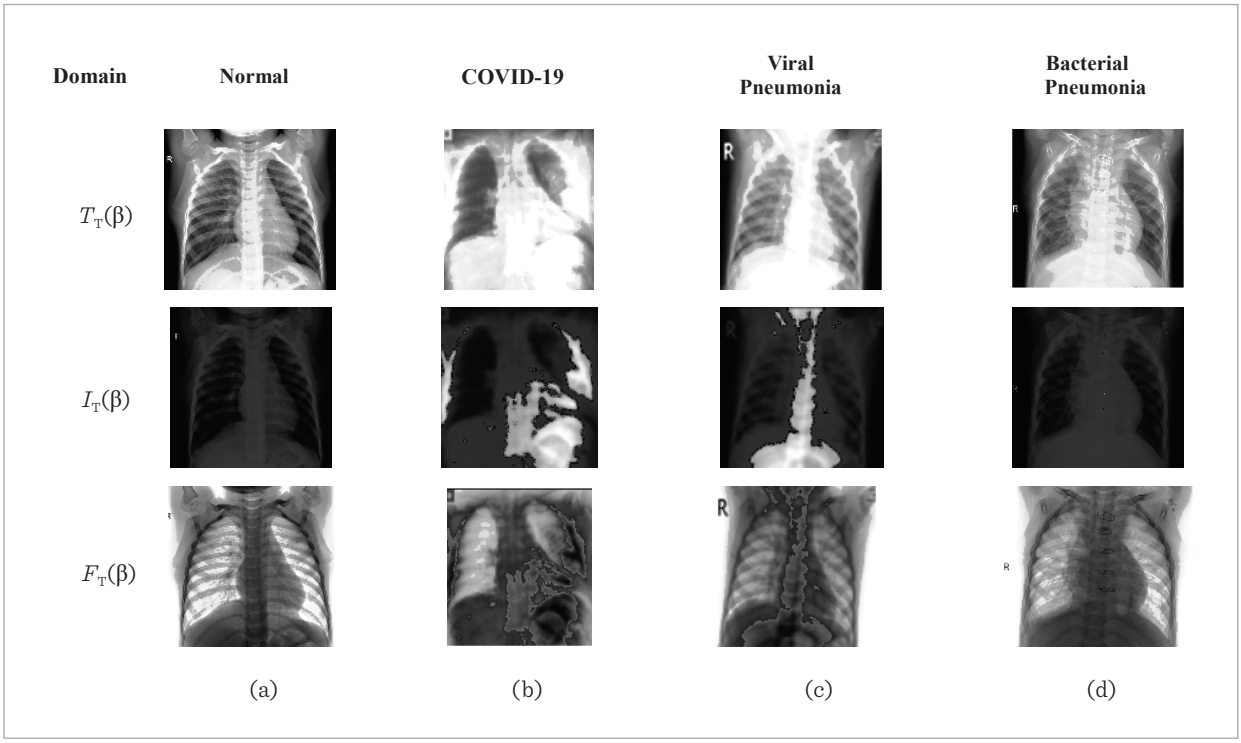

where,

$$\delta'(m,n) = abs(T_T'(m,n) - \overline{T_T}'(m,n))$$

$$\overline{T_T}'(m,n) = \frac{1}{w*w} \sum_{x=m-\frac{w}{2}}^{m+\frac{w}{2}} \sum_{y=n-\frac{w}{2}}^{n+\frac{w}{2}} T_T'(x,y). \quad (21)$$

The β-enhancement operation removes the noise and retains detailed information as shown in Figure 5 (a)-(d).

3.2. Deep Transfer Learning Model

The pre-processed beta-T images are then trained by taking advantage of the enhanced features. The training is done in three phases as depicted in Figure 6.

Phase 1: Initially, each input X-ray image is resized into three different scales. This is done using average pooling and it forms image pyramid and then each scaled version is travelled to the CNN model.

Phase 2: Detection task is done using a sliding window detector along the base network (Res-Net 50 [25], VGG-16 [14, 15], XG-Boost [27]).

a ResNet50: The model consists of 5 stages each with a convolution and identity block. Each convolution block has 3 convolution layers, and each identity block also has 3 convolution layers. The ResNet-50 has over 23 million trainable parameters and are faster to train and computationally less expensive.

b VGG-16: In this model the input image is passed through thirteen convolutional layers, five max pooling layers, and three dense layers which sum up to 21 layers but it has only sixteen weight layers i.e., learnable parameters layers. Though the accuracy results are good they are slow to train and hence consume high computational cost.

c XG-Boost: It is known as for extreme gradient boosting, it is a scalable, distributed gradient-boosted decision tree (GBDT) machine learn-

Algorithm 1: *Proposed Lung infection detection*

Input: *Medical Chest X-ray Image* $I_{X\text{-}img}$
Output: *Covid-19 Detection*
for *each image* $I_{X\text{-}img}$ *in dataset*
Convert to gray scale image
Transform the image into a neutrosophic fuzzy set P_{NS} *using Equations (4)-(7)*
Apply alpha mean operation on P_{NS} *using Equations (8)-(14).*
Perform beta enhancement operation on the True set $T_T(\alpha)$ *using Equations (15)-(21).*
for *each DTL model* ***do***
learning rate = 0.001
for *iteration = 1 to 50* ***do***
for $T_T^{`}(\beta)$ *in training dataset* ***do***
if *the miss-classification rate is increased for 10 iterations* ***then***
Update model learning rate
end
Update model coefficients
end
end
end
end
for *image in X-ray test dataset* ***do***
Classify the image and compute performance measures
end
for *image in Unseen dataset* ***do***
Classify the image into any of the category={Normal, COVID-19, Viral Pneumonia and Bacterial Pneumonia}
end

Figure 6
Proposed architecture model

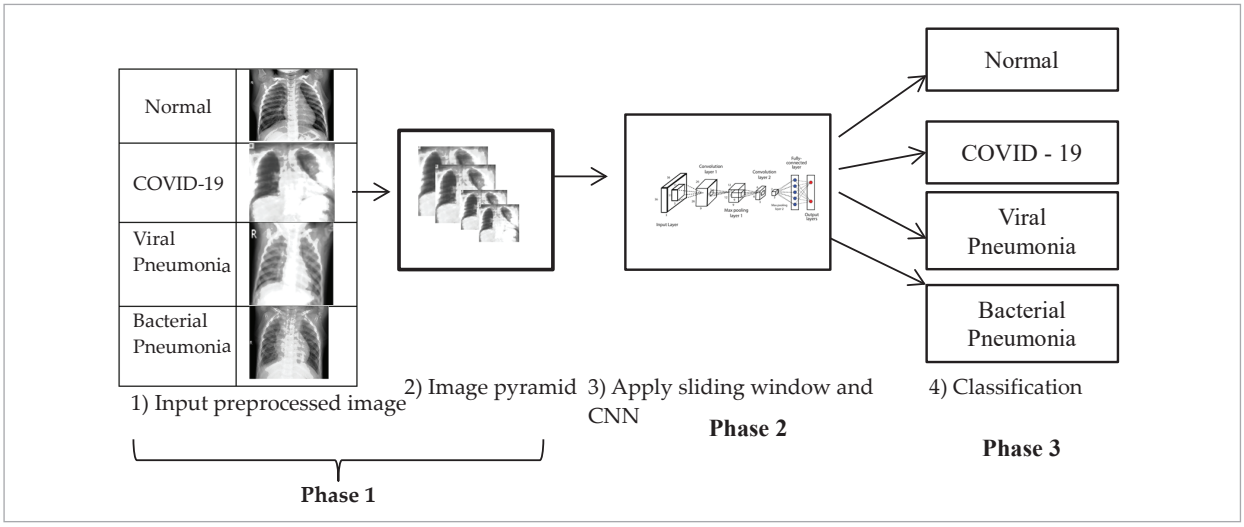

ing library used for classification. The model uses parallelization concept that reduces the training time to a greatly and achieves good prediction performance.

Phase 3: The outcomes are classified into a four-class classifier to determine the type of lung infection.

4. Experimental Results

4.1. Dataset

The X-ray dataset used for the proposed research are acquitted from Italian Society of Medical and Radio-paedia web [4]. The acquitted dataset contains about 306 images and are categorized into 4 types such as normal, pneumonia virus, bacterial pneumonia and COVID. For more dataset for training and testing set ActualMed COVID-19 Chest X-ray [6], RSNA Pneumonia Detection Challenge dataset [19], COVID radiography database [7] is used. The distribution of images and patient cases are portrayed as samples in Figure 2.

4.2. Experimental Set-up

Experiments are conducted in 10 different image sets such as (i) Original Chest X-ray dataset, (ii) The True (T), Indeterminacy (I) and Falsity (F) neutrosophic domain, (iii) The alpha True $\left(\overline{T_T}(\alpha)\right)$, alpha Indeterminacy $\left(\overline{I_T}(\alpha)\right)$ and alpha Falsity $\left(\overline{F_T}(\alpha)\right)$ neutrosophic domain, and (iv) The beta True $\left(\overline{T_T}(\beta)\right)$, beta Indeterminacy $\left(\overline{I_T}(\beta)\right)$ and beta Falsity $\left(\overline{F_T}(\beta)\right)$ neutrosophic domain. The images are downsized to 224 x 224 and to reduce the over fitting issue, augmentation is used to increase the dataset to improve the accuracy. Experiments are executed by performing augmentation techniques such as cropping, flipping, rotation and translation.

In augmentation through translation, it translates to [-30, 30] range while other techniques are freeze as it involves positional bias in the data leading to less accuracy. The experiments are executed in repeated ways by varying the meta-parameter values and the results are analyzed to produce the best version of the proposed work. Experiments are conducted with batch size to 32, 64 and 128 samples and the filter size ranges between 3, 5 and 7 are compared with the accuracy as depicted in Figure 8 (a). The graph summarizes an over fitting issue when the filter size is greater than 5. The feature map number was assigned as 200 and the activation functions such as ReLU, sigmoid, Softmax, and Tanh are used for comparisons. Learn-

Figure 7
Drop-out vs classification accuracy analysis for (a) ResNet-50 (b) VGG-16 (c) XG-Boost

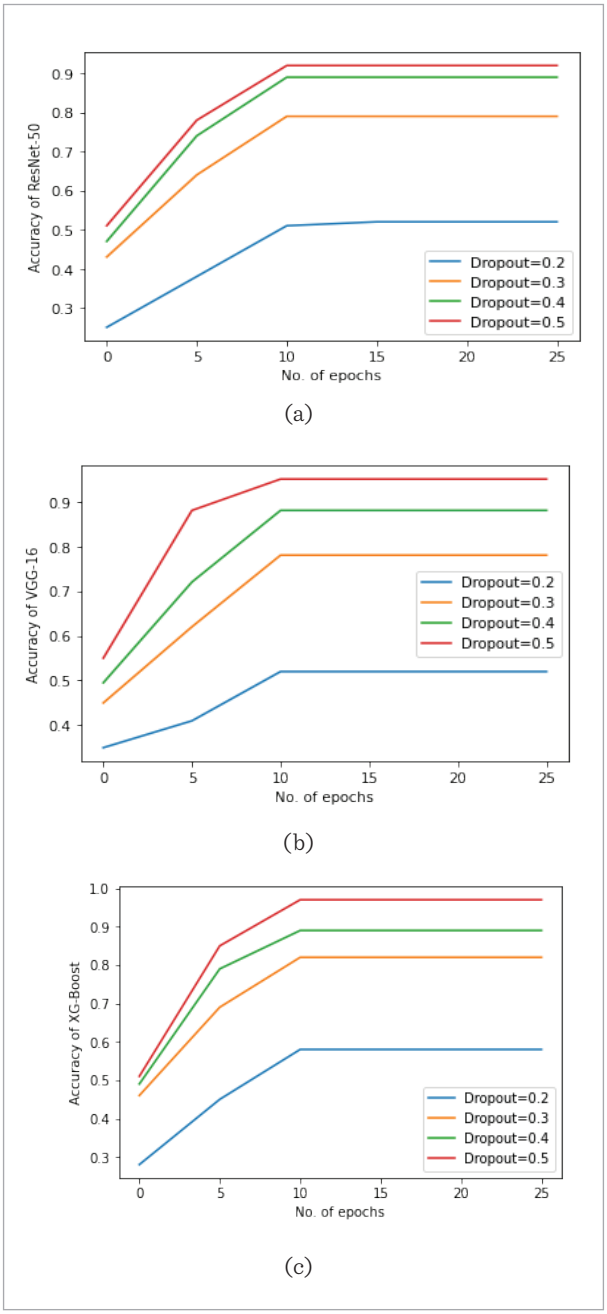

Figure 8
(a) Filter size vs classification accuracy (b) Learning rate vs classification accuracy

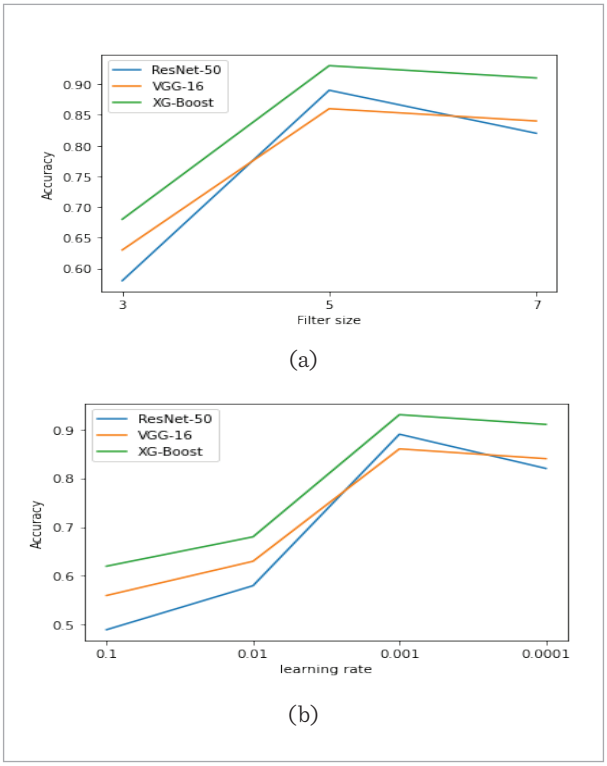

ing rate such as 0.1, 0.01, 0.001, and 0.0001 are compared for evaluation in Figure 8(b) and concludes a better accuracy is achieved at 0.001. Figure 7 depicts the accuracy analysis for dropout rate with 0.2, 0.3, 0.4, and 0.5 using ResNet-50, VGG-16 and XG-Boost and performance declines after 0.4. The multiclass cross entropy is used as loss function and the optimizer is experimented with Adaboost and AdaGrad, to provide a comprehensive analysis. Initially, the experiments are executed in 100 epochs with learning rate 0.0001 with a decay of 0.1 at 50 epochs and momentum 0.9.

The learning rate is reduced to 0.001 and the epochs are reduced to an optimal value of 10 epochs as shown in Figure 7 and 8 as an early stopping strategy to prevent over-fitting problems. The train-test split such as 70 – 30, 80 -20 and 90 – 10 are also executed.

From all the experimental analysis, the best hyper parameters are chosen for both training and testing stages: batch size - 32, momentum - 0.9, epochs - 10, learning rate - 0.001, optimizer – adaboost, training-testing split - 80% - 20%.

4.3. Performance Measures

1 Entropy

Entropy quantifies the image information content i.e., evaluation of the distribution of the intensity ranges. The more detailed information indicates higher clarity of the image leading to higher entropy value. For neutrosophic image entropy is calculated as the sum of individual entropies of T, I and F domain as shown in Equations (22)-(25) [11].

$$En_{NS} = En_T + En_I + En_F \tag{22}$$

$$En_T = -\sum_{i=\min\{T_T\}}^{\max\{T_T\}} p_T(i) \ln p_T(i) \tag{23}$$

$$En_I = -\sum_{i=\min\{I_T\}}^{\max\{I_T\}} p_I(i) \ln p_I(i) \tag{24}$$

$$En_F = -\sum_{i=\min\{F_T\}}^{\max\{F_T\}} p_F(i) \ln p_F(i) \tag{25}$$

where En_T, En_I, En_F are the entropies of T, I and $F_T(i)$, $p_I(i)$, $p_F(i)$ – probabilities of elements in T, I and F

2 Peak Signal-to-Noise Ratio

The qualitative way to analyze the enhanced image is done using Peak Signal-to-Noise Ratio (PSNR). It is defined as the ratio between the maximum possible value (power) of a signal and the power of distorting noise that affects the quality of its representation and is measured in decibels [23]. The mathematical representation of PSNR is defined using Equations (26)-(27).

$$PSNR = 20\log_{10}\left(\frac{MAX_f}{\sqrt{MSE}}\right) \tag{26}$$

$$MSE = \frac{1}{m*n}\sum_{0}^{m-1}\sum_{0}^{n-1}\left\|f(I,j) - g(I,j)\right\|^2 \tag{27}$$

where MAX_f represents the maximum pixel intensity value of the image. In our analysis, the MAX_f value used is 255. Here, f and g are two m × n monochrome images where one of the images is considered a noisy approximation compared to the other.

3 Sensitivity, Precision, Specificity, Accuracy and F1-Score

Performance measures such as sensitivity, precision, specificity, accuracy and F1- Score are used for determining type of lung infection. Sensitivity or recall is defined as the average detection rate and are formulated using Equation (28):

$$Sensitivity = \frac{TP}{TP + FN}. \tag{28}$$

Precision is defined as true positive rate, whereas specificity is true negative rate and is formulated using Equations (29)-(31) as follows:

$$Accuracy = \frac{TP + TN}{TP + TN + FP + FN} \tag{29}$$

$$Precision = \frac{TP}{TP + FP} \tag{30}$$

$$Specificity = \frac{TN}{TN + FP}, \tag{31}$$

where, TP is defined as the number of true positive identified its respective infection type and TN is defined as the number of true negative i.e., detecting the manually derived actual status.

FP is the number of false positives i.e., falsely detected the infection type, whereas FN is mentioned as the number of false negatives i.e., falsely identified. A frequent trade-off is noticed between the precision and recall of a detector and hence, the F1-score is used. It calculates the absolute performance of a detector, which makes comparisons easier [29]. The F1-score is defined in Equation (32) and is considered as the harmonic mean of the precision and recall [24]:

$$F1 - Score = 2 * \frac{1}{\frac{1}{recall} + \frac{1}{precision}}. \tag{32}$$

4 McNemar's Test [32]:

McNemar's Test is a statistical test performed to compare the predictive accuracy of any two methods and helps to improve the classification performance. The statistic is calculated using Equation (33):

$$F_{ij} = \frac{(f_{ij} - f_{ji})^2}{f_{ij} + f_{ji}}, \tag{33}$$

where, F_{ij} represents the pairwise statistical significance of difference between the accuracies of the two methods. f_{ij} expresses the number of samples which is classified correctly by ith method but wrongly by jth method, whereas f_{ji} denotes the number of samples correctly classified by jth method and falsely by ith method. The difference between two classifications is significant at the 95% confidence level (P = 0.05).

4.4. Experimental Results

To improve the robustness and effectiveness of the transformed neutrosophic chest X-ray images, T, I, F are enhanced using alpha and beta operations using Equations (2)-(21). The entropy of these images is calculated using Equations (22)-(25) signifies how much detailed information is extracted. Table 1 portrays an increase in entropy values of the X-ray images after alpha and beta operation.

Table 1
Entropy values of Images

Techniques	Entropy value
Chest X-ray Image	6.1455
Neutrosophic Image	18.8102
Alpha mean operation	19.1575
Beta enhancement operation	20.234

Peak Signal to Noise Ratio (PSNR) and Mean Square Error (MSE) are calculated between the images to assess their enhancement performance. Table 2 presents the results of PSNR and MSE values in each step of the enhancement process. The higher the PSNR value indicates better the image quality and hence after beta enhancement the PSNR values holds up to 75.15 dB when compared to original X-ray image.

Sensitivity, specificity, precision, F1-score accuracy and execution time values are shown in Tables 4-6 of the ResNet-50, VGG-16 and XGBoost model using open databases. It is observed that the proposed

Table 2
Values of PSNR and MSE parameters of the enhanced images

Techniques	Reference Image	MSE (dB)	PSNR (dB)
Neutrosophic Image	Chest X-ray Image	0.12	57.37
Alpha mean operation	Neutrosophic Image	0.04	62.14
Beta enhancement operation	Neutrosophic Image	0.022	64.74
Beta enhancement operation	Alpha mean operation	0.03	60.8
Beta enhancement operation	Chest X-ray Image	0.002	75.15

Table 3
McNemar's Statistical Test among the methods

i = Method1	j=Method2	f_{ij}	f_{ji}	*Fij*	P-value
Original Image	Beta T-Domain	82	15	46.28	1.02×10^{-11}
Neutrosophic Image	Beta T-Domain	72	13	40.95	1.56×10^{-10}
Alpha T Image	Beta T-Domain	42	8	23.12	1.52×10^{-5}

model on using ResNet-50 has good performace but has increase loss on comparison with other models, whereas VGG-16 has good outcomes but involves high computation cost. Analysis report concludes that the XGBoost model has achieved 97.33% accuracy and execution time of 3.32ms in detecting the corresponding type of lung infection. As shown by the test results, this detection method on Table 6 is more robust, fast execution with a very small number of false negatives.

XGBoost model has achieved better accuracy and execution time in detecting the corresponding type of lung infection. As shown by the test results, this detection method on Table 6 is considered to be more robust, fast execution with a very small number of false negatives. The training and the testing accuracy and loss are depicted in Figure 9 and 10 in different epochs. Figure 9 portrays that the XG-Boost has achieved 97.33% testing accuracy when compared to ResNet-50 with 92.67% and VGG-16 with 95.3%. Figure 10 shows the loss of XG-Boost is about 0.172 at epoch 10 and comparatively less than ResNet-50 with 0.35 and VGG-16 with 0.28.

The proposed framework is then compared with other existing frameworks on open datasets and depicted in Figure 11. The existing work [22] focuses on training and testing the neutrosophic T, I, F domain of Chest X-ray. Elasnaoui [9] used input X-ray images and performs augmentation increasing the size of the dataset and trains using CheXNet and DenseNet201.

Table 4
Sensitivity, specificity, precision, F1-score, accuracy and time values of ResNet-50

	Performance Metrics (%) of ResNet-50					
	Sensitivity	Precision	Specificity	Accuracy	F1 Score	Time (ms)
Original	69.68	75.52	75.86	72.67	72.48	5.82
T-Domain	72.59	59.39	59.39	65.33	65.33	4.21
I-Domain	66.67	56.41	59.52	62.67	61.11	4.18
F-Domain	68.89	57.41	58.18	63	62.63	4.15
Alpha-T	78.87	80	82.28	80.67	79.43	4.12
Alpha-I	72.41	73.43	75.48	74	72.92	4.08
Alpha-F	70.97	80.88	82.07	76.33	75.6	4.15
Beta-T	91.46	94.94	94.12	92.67	93.17	4.02
Beta-I	84.91	88.24	87.23	86	86.54	4.32
Beta-F	88.62	93.67	92.48	90.33	91.08	4.08

Table 5
Sensitivity, specificity, precision, F1-score, accuracy and time values of VGG-16

	Performance Metrics (%) of VGG-16					
	Sensitivity	Precision	Specificity	Accuracy	F1 Score	Time(ms)
Original	72.39	82.52	81.75	76.67	77.12	8.21
T-Domain	71.11	57.49	56.97	63.33	63.58	7.55
I-Domain	66.92	57.05	59.88	63	61.59	6.78
F-Domain	69.63	58.02	58.79	63.67	63.3	7.26
Alpha-T	80.14	81.29	83.65	82	80.71	7.01
Alpha-I	74.65	72.6	74.68	74.67	73.61	6.23
Alpha-F	71.34	80.58	81.12	76	75.68	7.11
Beta-T	94.77	97.02	96.09	95.33	95.88	7.33
Beta-I	85.63	88.96	87.86	86.67	87.26	6.02
Beta-F	93.29	93.87	92.65	93	93.58	7.41

Figure 9
Training and Testing Accuracy for (a)ResNet-50 (b)VGG-16 (c) XG-Boost

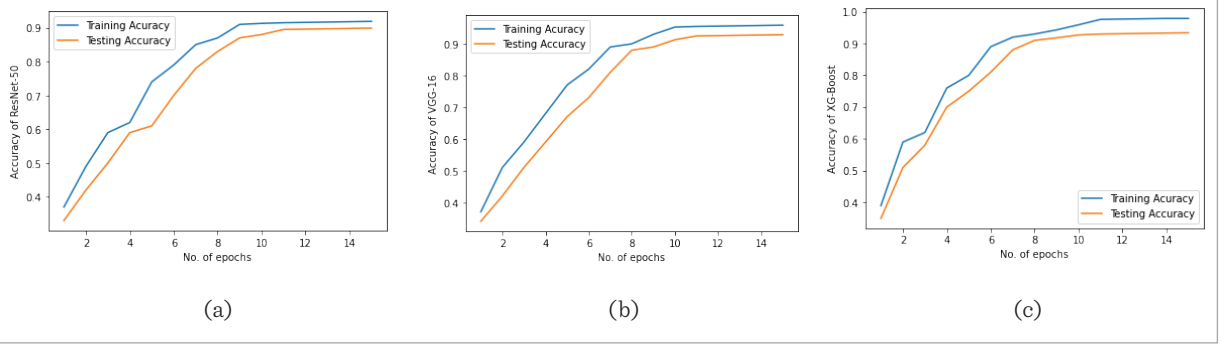

(a) (b) (c)

Figure 10
Training and Testing Loss for (a)ResNet-50 (b)VGG-16 (c) XG-Boost

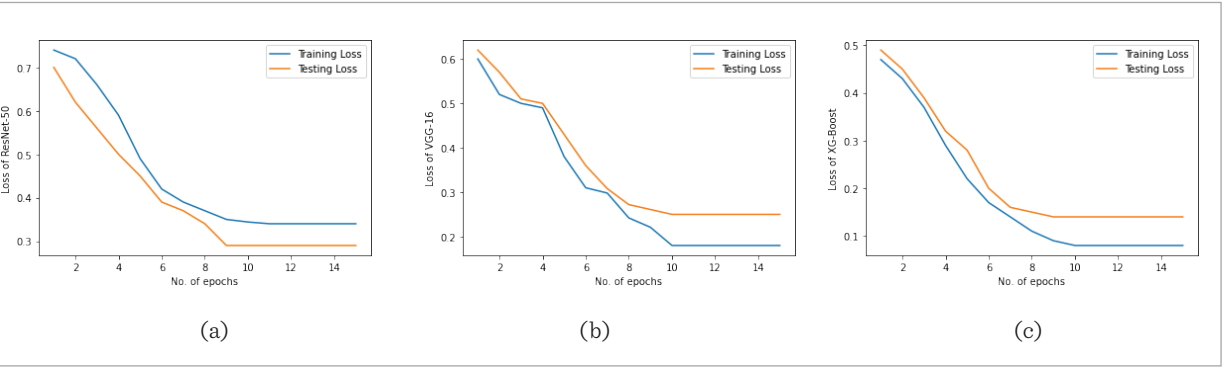

(a) (b) (c)

Table 6
Sensitivity, specificity, precision, F1-score, accuracy and time values of XG-Boost

	Performance Metrics (%) of XG-Boost					
	Sensitivity	Precision	Specificity	Accuracy	F1 Score	Time(ms)
Original	73.01	85	84.67	78.33	78.55	4.82
T-Domain	71.94	59.88	58.39	64.67	65.36	3.92
I-Domain	67.41	57.96	60	63.33	62.33	3.89
F-Domain	70.29	61.01	61.73	65.67	65.32	3.95
Alpha-T	84.91	95.74	95.74	90	90	3.5
Alpha-I	74.65	72.6	74.68	74.67	73.61	3.43
Alpha-F	77.84	88.44	87.22	82	82.8	3.67
Beta-T	97.14	98.27	97.6	97.33	97.7	3.32
Beta-I	85.8	90.85	89.86	87.67	88.25	3.26
Beta-F	97.56	95.24	94.12	96	96.39	3.39

Khan [16] classifies the normal, Pneumonia-viral and Covid-19 chest x-ray images using Xception architecture and Ucar [27] uses DenseNet121 for Covid-19 detection.

A statistical test is performed on XG-Boost model using various inputs (original, neutrosophic and alpha images) using Equation (32) and is compared with beta T-domain images to determine the best method as shown in Table 3. If the P value with degree of Freedom (DoF=1) for the McNemar's test of overall significance is less than your significance level (P=0.05), the null-hypothesis is rejected and concluded that proposed model provides a better fit. It concludes that the proposed Beta-T domain works better than other methods and the test results has significant differences in the classification accuracy between them.

Figure 11 signifies that the proposed enhanced neutrosophic image outperform these performances in terms of accuracy.

Figure 11
Accuracy obtained and compared with other state-of-art methods

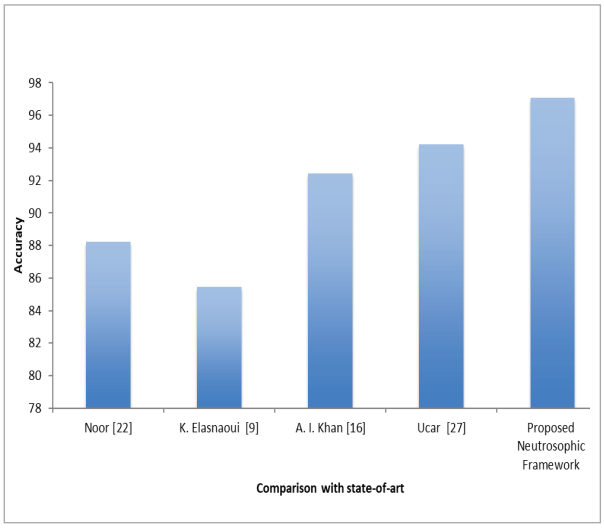

5. Conclusion

In the rapid evolving global pandemic of COVID-19 for past years has led to misinterpretation of other lung infections such as Viral Pneumonia, Bacterial Pneumonia and hence the need of an automated approach to detection has become a primary demand. The variation in the lung infections is based on the volume of lung opacity and hence each pixel plays a vital role to determine its types. Thus, the neutrosophic set is proposed as it improves the quality of images with the usage of indeterminacy. The imag-

es are converted to neutrosophic domain and then enhanced using alpha and beta enhancement techniques. The enhanced neutrosophic sets are then fed to deep learning models such as Resnet-50, VGG-16 and XG-Boost. Experimental analysis is done using transfer learning by varying many meta-parameters to conclude the best parameters for these models. On analysis, the proposed network demonstrates that the beta T-domain image on XG-Boost with accuracy of 97.33% achieves a better accuracy with loss of 0.172 and good computation time of 3.32ms.

The major limitation of the proposed work is the limited availability of images to train AI-based models and the usage of the complete lung image without localizing the lung opacity regions as this approach can further reduce time and improve efficiency. The future work will concentrate on focusing on large datasets and segmenting the localized lung area to feed to CNN models. The proposed model can be elevated as a diagnosis usability tool for radiologists and doctors for lung infected patients.

References

1. Alqudah, A. M., Qazan, S., Hiam, A., Quasmieh, I. A., Amin, A. COVID-19 Detection from X-ray Images Using Different Artificial Intelligence Hybrid Models. Jordan Journal of Electrical Engineering, 2020, 6 (2), 168-178. https://doi.org/10.5455/jjee.204-1585312246
2. Ayan, E., Ünver, H. M., Diagnosis of Pneumonia from Chest X-Ray Images Using Deep Learning. Scientific Meeting on Electrical-Electronics Biomedical Engineering and Computer Science (EBBT), Istanbul, Turkey, 2019, 1-5. https://doi.org/10.1109/EBBT.2019.8741582
3. Barstuğan, M., Özkaya, U., Öztürk, Ş. Coronavirus (COVID-19) Classification Using CT Images by Machine Learning Methods, 2020, 2003.09424. https://doi.org/10.48550/arxiv.2003.09424
4. Chouhan V., Singh S. K., Khamparia A., Gupta D., Tiwari P., Moreira C., Damaševičius R., de Albuquerque VHC. A Novel Transfer Learning Based Approach for Pneumonia Detection in Chest X-ray Images. Applied Sciences, 2020, 10(2), 559, 1-17. https://doi.org/10.3390/app10020559
5. Christianto, V, Smarandache, F. A Review of Seven Applications of Neutrosophic Logic. Cultural Psychology, Economics Theorizing, Conflict Resolution, Philosophy of Science, 2019, 2, 128-137. https://doi.org/10.3390/j2020010
6. Chung, A. Actualmed COVID-19 Chest X-ray Data Initiative. https://github.com/agchung/Actualmed-COVID-chestxray-dataset
7. Cohen J. P., Morrison P., Dao L., COVID-19 Image Data Collection. arXiv:2003.11597, 2020. https://doi.org/10.48550/arXiv.2003.11597
8. Dawid Połap, Włodarczyk-Sielicka, M., Wawrzyniak, N. Automatic Ship Classification for a Riverside Monitoring System Using a Cascade of Artificial Intelligence Techniques Including Penalties And Rewards. ISA Transactions, 2022, 121, 232-239. https://doi.org/10.1016/j.isatra.2021.04.003
9. Elasnaoui, K., Chawki, Y. Using X-Ray Images and Deep Learning for Automated Detection of Coronavirus Disease, Journal of Biomolecular Structure and Dynamics, 2020, 39(10), 3615-3626. https://doi.org/10.1080/07391102.2020.1767212
10. Ghiass, R., Hakim, B., Maldague, X. Université Laval Face Motion and Time-Lapse Video Database (ULFMTV), 2018.
11. Guo, Y., Cheng, H. D. A New Neutrosophic Approach to Image Denoising. New Mathematics and Natural Computation, 2009, 5(3), 653-662. https://doi.org/10.1142/S1793005709001490
12. Guo, Y., Cheng, H. D. New Neutrosophic Approach to Image Segmentation. Pattern Recognition, 2009, 42(5), 587-95. https://doi.org/10.1016/j.patcog.2008.10.002
13. Hemdan, E. E. D., Shouman, M. A., Karar, M. E. CovidxNet: A Framework of Deep Learning Classifiers to Diagnose Covid-19 in X-Ray Images, 2020, 1. https://doi.org/10.48550/arxiv.2003.11055
14. Kamal, K. C., Yin, Z., Wu, M., Wu, Z. Evaluation of Deep Learning-Based Approaches for COVID-19 Classification Based on Chest X-Ray. Images, Signal, Image and Video Processing, 2021, 15(11), 1-8. https://doi.org/10.1007/s11760-020-01820-2
15. Kermany, D. S., Goldbaum, M., Cai, W., Valentim, C. C. S., Liang, H., Baxter, S. L., McKeown, A., Yang, G., Wu, X., Yan, F. Identifying Medical Diagnoses and Treatable Diseases by Image-Based Deep Learning. Cell, 2018, 172 (5), 1122-1131. https://doi.org/10.1016/j.cell.2018.02.010

16. Khan, A. I., Shah, J. L., Bhat, M. M. Coronet: A Deep Neural Network for Detection and Diagnosis Of COVID-19 From Chest X-Ray Images. Computer Methods and Programs in Biomedicine, 2020, 196. https://doi.org/10.1016/j.cmpb.2020.105581

17. Klington, A. G., Ramesh, K., Kadry, S. Cost-Effective Watermarking Scheme for Authentication of Digital Fundus Images in Healthcare Data Management. Information Technology and Control, 2021, 50(4), 645-655. https://doi.org/10.5755/j01.itc.50.4.28957

18. Kuei-Hu, C. A Novel Risk Ranking Method Based on The Single Valued Neutrosophic Set. Journal of Industrial & Management Optimization, 2022, 18(3), 2237-2253. https://doi.org/10.3934/jimo.2021065

19. Radiological Society of North America. COVID-19 radiography database. https://www.kaggle.com/tawsifurrahman

20. Smarandache, F. A Unifying Field in Logics: Neutrsophic Logic, Neutrosophy, Neutrosophic Set, Neutrosophic Probability (Fourth Edition), University of New Mexico, 2002, 332, 5-21.

21. Smarandache, F. A Unifying Field in Logics Neutrosophic Logic. Neutrosophy, Neutrosophic Set, Neutrosophic Probability, American Research Press, 2003.

22. Smarandache, F, Khalifa, N. E. M., Manogaran, G., Loey, M. A Study of the Neutrosophic Set Significance on Deep Transfer Learning Models: an Experimental Case on a Limited COVID-19 Chest X-ray Dataset.Cognitive Computation, 2020. https://doi.org/10.1007/s12559-020-09802-9

23. Sofia Jennifer, J., Sree Sharmila, T., Srinivasan R, Facial Feature Extraction for Head Tilt Images Based on Eye Canthus, IEEE TENCON, 2016, 566-570. https://doi.org/10.1109/TENCON.2016.7848064

24. Sofia Jennifer, J., Sree Sharmila, T. Real Time Blink Recognition from Various Head Pose Using Single Eye. Multimedia Tools and Applications, 2018, 77, 31331-31345. https://doi.org/10.1007/s11042-018-6113-3

25. Shi, H., Han, X., Jiang, N. Radiological Findings from 81 Patients with COVID-19 Pneumonia in Wuhan, China: A Descriptive Study. The Lancet Infectious Diseases, 2020, 20(4), 425-434. https://doi.org/10.1016/S1473-3099(20)30086-4

26. Toussie, D., Voutsinas, N., Finkelstein, M. Clinical and Chest Radiography Features Determine Patient Outcomes in Young and Middle-Aged Adults with COVID-19. Radiology, 2020, 297(1), 197-206. https://doi.org/10.1148/radiol.2020201754

27. Ucar, F., Korkmaz, D. Covidiagnosis-Net: Deep Bayes-Squeezenet Based Diagnosis of the Coronavirus Disease 2019 (COVID-19) from X-Ray Images. Medical Hypotheses, 2020, 140. https://doi.org/10.1016/j.mehy.2020.109761

28. Zhang, J., Xie, Y., Li, Y., Shen, C., Xia, Y. COVID-19 Screening on Chest X-ray Images Using Deep Learning Based Anomaly Detection. Molecular Biology, 2020. https://doi.org/10.48550/arxiv.2003.12338.

29. Zhang, M., Zhang, L., Cheng, H. D. A Neutrosophic Approach to Image Segmentation Based on Watershed Method. Signal Processing, 2010, 90 (5), 1510-1517. https://doi.org/10.1016/j.sigpro.2009.10.021

30. Zhang, W., Li, X., Ma, H., Luo, Z., Li, X. Federated Learning for Machinery Fault Diagnosis with Dynamic Validation and Self-Supervision, Knowledge-Based Systems, 2021, 213. https://doi.org/10.1016/j.knosys.2020.106679